Why Does *trans*-Azobenzene Have a Smaller Isomerization Yield for $\pi\pi^*$ Excitation Than for $n\pi^*$ Excitation?

Shuai Yuan,[†,‡] Yusheng Dou,*[,‡,§] Weifeng Wu,[‡] Yun Hu,[‡] and Jianshe Zhao[†]

Key Laboratory of Synthetic and Natural Functional Molecule Chemistry of Ministry of Education, Shaanxi Key Laboratory of Physico—Inorganic Chemistry, Department of Chemistry, Northwest University, Xi'an, 710069, China, Institute of Computational Chemistry, Chongqing University of Posts and Telecommunications, Chongqing, 400065, China, and Department of Physical Sciences, Nicholls State University, P.O. Box 2022, Thibodaux, Louisiana 70310

Received: July 14, 2008; Revised Manuscript Received: August 18, 2008

A realistic dynamics simulation study is reported for the photoisomerization of trans-azobenzene. The isomerization follows both $n\pi^*$ (the HOMO → LUMO) and $\pi\pi^*$ (the HOMO−1 → LUMO) excitations. The simulation finds that for the $\pi\pi^*$ excitation, the relaxation of the S($\pi\pi^*$) state is immediately followed by double excitation, $(\pi)^2(\pi^*)^2$. The decay from the S($(\pi)^2(\pi^*)^2$) state to the S_0 state can occur at partially twisted structure, which favors the formation of the trans isomer. Multiple decay channels are found at about twisted structure for both $n\pi^*$ and $\pi\pi^*$ excitations. Decay at about twisted geometry leads to the formation of either cis or trans isomer. Opening of the decay channel at partially twisted structure accounts for the smaller isomerization yield for the $\pi\pi^*$ excitation.

Introduction

Azobenzene (Ab) has two stable forms, namely the cis (*Z*) and trans (*E*) isomers. When subjected to ultraviolet or visible radiation, Ab undergoes $E \leftrightarrow Z$ isomerization. This makes Ab and its derivatives excellent candidates for many applications,[1−3] including molecular switches, image storage devices, as well as the recently designed light-driven molecular shuttle.[4] Therefore there has been extensive interest in the photophysical and photochemical behavior of Ab.

Although the photoisomerization of Ab can start from either the *Z* or *E* isomer, the quantum yield of the reaction is different for two different processes.[5] It was found that the quantum yield for both processes depends on the excitation wavelength and solvents:[5] In *n*-hexane, a nonpolar solvent, the $Z-E$ quantum yield is 0.56 for the $n\pi^*$ excitation (S_1 state) and 0.27 for the $\pi\pi^*$ excitation (S_2 state).[3,6] The $E-Z$ quantum yields are 0.25 on the S_1 state and 0.11 on the S_2 state.[7] In polar solvents, such as ethanol, the quantum yield ratio of the $E \rightarrow Z$ over the $Z \rightarrow E$ changes significantly. However, the ratio between two excitations is about the same. The quantum yields of two excitations for both processes differ up to a factor of 2, indicating the violation of the Kasha rule, which states that the quantum yield is independent of the excitation energy.

To understand the wavelength dependence of the quantum yield, it has been proposed that the reaction proceeds differently on two different electronically excited states: the reaction follows an inversion path for the $n\pi^*$ excitation and rotation path for the $\pi\pi^*$ excitation.[5,8] On the basis of this assumption, Rau successfully rationalized the observed two different quantum yields for two different excitations of the free Ab molecule. This proposal then has been a dominant model in the interpretation of experimental results[9−14] and has guided some theoretical investigations.[5] A very recent Resonance Raman spectroscopic experiment[15] also favors the inversion path. On the other hand, the inversion mechanism for the $\pi\pi^*$ excitation is not supported by recent theoretical calculations, including first-principles constrained density-functional calculations[16] and CASSCF level calculations[17−19] and is also in contradiction with recent new experimental observations.[20]

By studying the transient Raman and absorption spectrum, Fujino et al.[21] found that almost all molecules excited to the S($\pi\pi^*$) state immediately decay to the S($n\pi^*$) state and that the isomerization following the $\pi\pi^*$ excitation takes place after the S($\pi\pi^*$) → S($n\pi^*$) electronic relaxation. They concluded that the isomerization mechanism for the $\pi\pi^*$ and $n\pi^*$ excitations should be the same. On the basis of the previous suggestion that the inversion path predominates in the isomerization in the S($n\pi^*$) state, they concluded that for both excitations, the reaction follows the inversion coordinate.

On the other hand, fluorescence anisotropy measurements in hexane[22] demonstrate that the photoisomerization in the S($n\pi^*$) state follows the NN torsion path. Many high level quantum chemical calculations also suggest that the photoisomerization in the S($n\pi^*$) state is dominated by the torsion path. Particularly, the calculations at CASSCF and CASPT2[23] levels find that the S($n\pi^*$) minimum energy path (MEP) follows the rotation path for both isomers.

To explain the smaller photoisomerization yield found for the $\pi\pi^*$ excitation than for the $n\pi^*$ excitation, Fujino et al.[21] proposed that the lower photoisomerization quantum yield for the $\pi\pi^*$ excitation is due to either a smaller isomerization yield for the hot S($n\pi^*$) state produced in the S($\pi\pi^*$) → S($n\pi^*$) relaxation than for the cold S($n\pi^*$) state or in addition to at the inverted geometry, the hot S($n\pi^*$) state decays to the S_0 state also at the reactant geometry, which lowers isomerization quantum yield. Very recently, Orlandi and co-workers[24] performed ab initio CASSCF and CASPT2 calculation for the S($\pi\pi^*$) photoisomerization. They find that a doubly excited state, denoted as S($(\pi)^2(\pi^*)^2$), plays an important role in the

* Corresponding author. Phone: 1 985 448 4880. Fax: 985 448 4927. E-mail address: Yusheng.Dou@nicholls.edu.
† Northwest University.
‡ Chongqing University of Posts and Telecommunications, Chongqing.
§ Nicholls State University.

10.1021/jp806227x CCC: $40.75
Published on Web 11/19/2008

S($\pi\pi^*$) relaxation. This intermediate state drives the photoisomerization following the rotation path and also induces fast internal conversion to the S(nπ^*) state at the different CNNC torsion. The authors propose that these features are responsible for the smaller photoisomerization yield as well as other properties of the S($\pi\pi^*$) decay pathway and photoreactivity.

Clearly, the wavelength dependence of the Ab photoisomerization yield is not well understood. Although theoretical quantum calculations are fundamental important in understanding the main features of the mechanisms behind the Ab photoisomerization, the static calculations alone cannot provide detailed information on the mechanism because they do not solve the time-dependent Schrödinger equation and therefore are incapable of describing the time-dependent process of the photoisomerization.

In this paper, we present the dynamics simulation study of the *E*-Ab photoisomerization by a semiclassical approach. The simulation follows both the nπ^* and $\pi\pi^*$ excitations induced by two 50 fs (fwhm) laser pulses which are different in the photon energies, and we find that for the $\pi\pi^*$ excitation the S(nπ^*) state coming from the S($\pi\pi^*$) $\rightarrow$ S(nπ^*) conversion can relax to the S_0 state at either the twisted or the partially twisted geometries. The twisted geometry is defined as one with the CNNC = 90° and the partially twisted geometry is defined as one with the CNNC being about 135°, the midpoint between 180° and 90°. The decay at the partially twisted structure favors the formation of the *E*−*E* and lowers the *E*−*Z* isomerization yield.

Methodology

A semiclassical method is employed to study the photoisomerization of *E*-Ab. In this approach, the state of the valence electrons is calculated by the time-dependent Schrödinger equation, but the radiation field and the motion of the nuclei are treated classically. According to time-dependent perturbation theory, such a semiclassical treatment effectively includes effective "*n*-photon" and "*n*-phonon" processes in absorption and stimulated emission.

A detailed description of this technique has been published elsewhere,[25,26] and only a short explanation is given here. The one-electron states are obtained at each time step by solving the time-dependent Schrödinger equation in a nonorthogonal basis,

$$i\hbar\frac{\partial\Psi_j}{\partial t} = \mathbf{S^{-1}}\cdot\mathbf{H}\cdot\Psi_j \qquad (1)$$

where **S** is the overlap matrix for the atomic orbitals. The laser pulse is characterized by the vector potential **A**, which is coupled to the Hamiltonian through the time-dependent Peierls substitution[27]

$$H_{ab}(\mathbf{X}-\mathbf{X}') = H^0_{ab}(\mathbf{X}-\mathbf{X}')\exp\left(\frac{iq}{\hbar c}\mathbf{A}\cdot(\mathbf{X}-\mathbf{X}')\right) \qquad (2)$$

Here $H_{ab}(\mathbf{X}-\mathbf{X}')$ is the Hamiltonian matrix element for basis functions *a* and *b* on atoms at **X** and **X′** respectively, and $q = -e$ is the charge of the electron.

The electronic states were calculated with a density-functional-based method that is described in detail elsewhere[28,29] and that has essentially the same strengths and limitations as TDDFT. In particular, the bonding is well-described but the excited-state energies are typically too low. For this reason, as is conventional, we matched the effective central photon energy of the laser pulse to the relevant density-functional (rather than experimental) excitation energy and this should not have a significant effect in the interpretation of the results. This same model has been used to study several photochemical reactions and was found to yield good descriptions of molecular response to ultrashort laser pulses. The examples include that the explanation of the nonthermal fragmentation of C_{60}[30] is in good agreement with experimental observations, the simulation of the formation of the tetramethylene[31] intermediate diradical is consistent with time-of-flight mass spectrometry measurements, and the characterization of the geometry changes at some critical points[32] is compatible with molecular mechanics valence bond calculations.

In this model, the nuclear motion is solved by the Ehrenfest equation of motion

$$M_l\frac{d^2X_{l\alpha}}{dt^2} = -\frac{1}{2}\sum_j\Psi_j^+\cdot\left(\frac{\partial\mathbf{H}}{\partial X_{l\alpha}} - i\hbar\frac{1}{2}\frac{\partial\mathbf{S}}{\partial X_{l\alpha}}\cdot\frac{\partial}{\partial t}\right)\cdot\Psi_j - \partial U_{rep}/\partial X_{l\alpha} \qquad (3)$$

where U_{rep} is the effective nuclear−nuclear repulsive potential and $X_{l\alpha} = \langle\hat{X}_{l\alpha}\rangle$ is the expectation value of the time-dependent Heisenberg operator for the α coordinate of the nucleus labeled by *l* (with $\alpha = x, y, z$). Equation 3 is obtained by neglecting the terms of second and higher order in the quantum fluctuations $\hat{X} - \langle\hat{X}_{l\alpha}\rangle$ in the exact Ehrenfest theorem.

A unitary algorithm obtained from the equation for the time evolution operator[33] is used to solve the time-dependent Schrödinger equation (eq 1). Equation 3 is numerically integrated with the velocity Verlet algorithm. A time step of 50 as was selected and energy conservation was then found to hold to better than 1 part in 10^6 in a 1 ps simulation for *E*-Ab at 298 K.

The present "Ehrenfest" approach is complementary to other methods based on different approximations, for example, the full multiple spawning model developed by the Martinez group.[34] The weakness of this method is that it amounts to averaging over all the terms in the Born−Oppenheimer expansion,[35−39]

$$\Psi^{total}(X_n,x_e,t) = \sum_i\Psi_i^n(X_n,t)\,\Psi_i^e(x_e,X_n) \qquad (4)$$

rather than following the time evolution of a single term (i.e., a single potential energy surface), which is approximately decoupled from all the others.[37−42] (Here X_n and x_e represent the sets of nuclear and electronic coordinates respectively, and the Ψ_i^e are eigenstates of the electronic Hamiltonian at fixed X_n.) The strengths of the present approach include that it retains all of the 3*N* nuclear degrees of freedom (instead of only the 2 or 3 that are typically considered in a potential-energy-surface calculation) and it incorporates both the excitation due to a laser pulse and the subsequent de-excitation at an avoided crossing near a conical intersection.

Results and Discussion

The ground-state geometry of *E*-Ab, which is obtained after 1000 fs simulation at the room temperature, has an approximately planar structure with C_{2h} symmetry at its equilibrium configuration. The geometry parameters, including the bond lengths, bond angles, and dihedral angles as well as energies are found to be consistent with published results.[43−46] This ground-state geometry is used for all simulations in this study.

Many molecular orbitals are involved in the laser excitation but HOMO−1, HOMO, and LUMO are of particular interest. Each of these orbitals can be characterized by the predominant feature of the NN double bond: the HOMO−1 exhibits appreciable π bonding, the HOMO displays n nonbonding lone

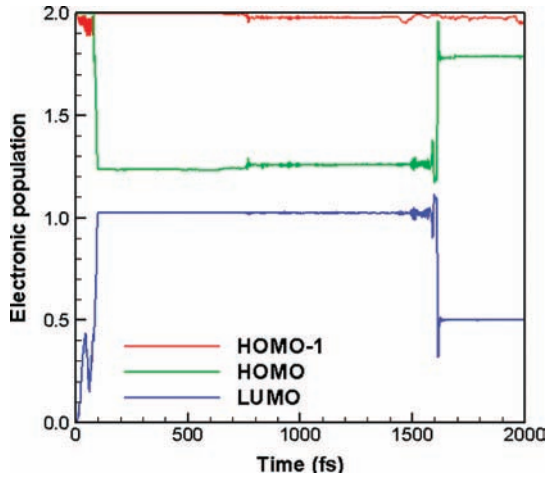

Figure 1. Variation with time of the electronic populations of the HOMO−1, HOMO, LUMO of *E*-Ab following application of a 50 fs (fwhm) laser pulse with a fluence of 0.459 kJ/m^2 and photon energy of 1.75 eV. This laser pulse induces the nπ* excitation.

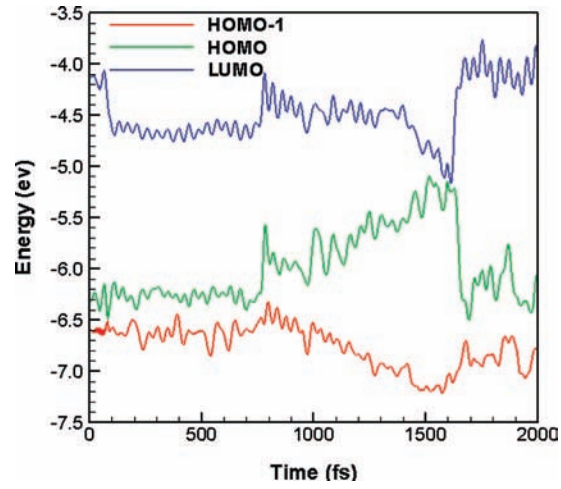

Figure 2. Energy variation with time of the HOMO−1, HOMO and LUMO of *E*-Ab following application of a 50 fs (fwhm) laser pulse with a fluence of 0.459 kJ/m^2 and photon energy of 1.75 eV. This laser pulse induces the nπ* excitation.

pairs, and the LUMO shows apparent π* antibonding. On the basis of the characters of these orbitals, we interpret the HOMO → LUMO excitation as nπ* excitation, the HOMO−1 → LUMO excitation as $\pi\pi$* excitation, the HOMO−1 → HOMO hole excitation as S($\pi\pi$*) decay, HOMO → LUMO double excitation as $(\pi)^2(\pi^*)^2$ excitation*.

1. nπ Excitation. To produce nπ excitation, a 50 fs (fwhm) laser pulse was applied with an effective photon energy of 1.75 eV. The energy was found to produce a best laser excitation. Simulations were run for several tens of trajectories to determine an appropriate laser fluence for the reaction. The laser fluences studied range from about 1.0 to 0.05 kJ/m^2 with different steps. The simulations found that a suitable laser power for the reaction is 0.459 kJ/m^2. Others either produce fragmentations due to multiple electronic excitations or no reactions because of very small amount of electrons being excited. Few trajectories with different initial geometries were simulated for the laser fluence of 0.459 kJ/m^2 and no inconsistent results were observed. For this reason only one representative trajectory will be presented.

The time-dependent populations of the HOMO−1, HOMO and LUMO are presented in Figure 1. The laser pulse pumps about 1.0 electron mainly from the HOMO to the LUMO by the end of the laser excitation. This nπ* excitation promotes the molecule to the electronically excited state. The most remarkable electronic transition from the LUMO to HOMO is observed at 1620 fs, which essentially leads the excited molecule to the ground state.

The variations with time of the energies of the HOMO−1, HOMO and LUMO are plotted in Figure 2. The energy gap between the HOMO and LUMO decreases noticeably soon after the laser pulse is incorporated. It remains about a constant value from 120 fs to about 710 fs. The gap after then shrinks significantly mainly because of the increase in the energy of the HOMO. One avoided crossing between the HOMO and LUMO is found at 1620 fs, which is responsible for the nonadiabatic transition of the excited molecule to the ground state. Soon after this avoided crossing, the energy gap comes to 2.4 eV, which is about the same as its initial value, and then vibrates about this value for the rest of the simulation time.

Figure 3 shows six snapshots taken at different times of the simulation. Starting from the equilibrium geometry in the electronic ground-state at 0 fs, *E*-Ab is electronically excited by the laser pulse and starts to rotate about the central bond

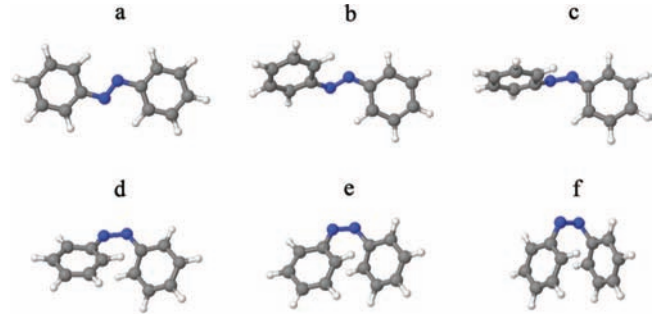

Figure 3. Six snapshots taken from the simulation of *E*-Ab responding to a 50 fs (fwhm) laser pulse with a fluence of 0.459 kJ/m^2 and photon energy of 1.75 eV at (a) 0 fs, (b) 1286 fs, (c) 1616 fs, (d) 1696 fs, (e) 1727 fs, and (f) 1772 fs. The simulation follows the nπ* excitation.

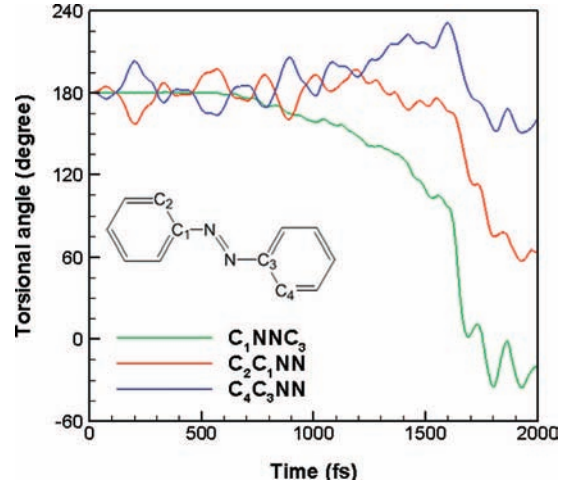

Figure 4. Variations with time of three torsional angles of *E*-Ab subjected to a 50 fs (fwhm) laser pulse with a fluence of 0.459 kJ/m^2 and photon energy of 1.75 eV. The laser pulse produces the nπ* excitation.

before 600 fs. It continuous this rotation until the formation of the *Z*-isomer after 1200 fs.

The variations of three torsional angles with time are plotted in Figure 4. The molecule does not take obvious rotation around either the N−N bond or any of two C−N bonds before 550 fs. It starts to rotate around the N−N bond after 600 fs and becomes the *Z*-isomer after 1620 fs when the C−N−N−C dihedral angle

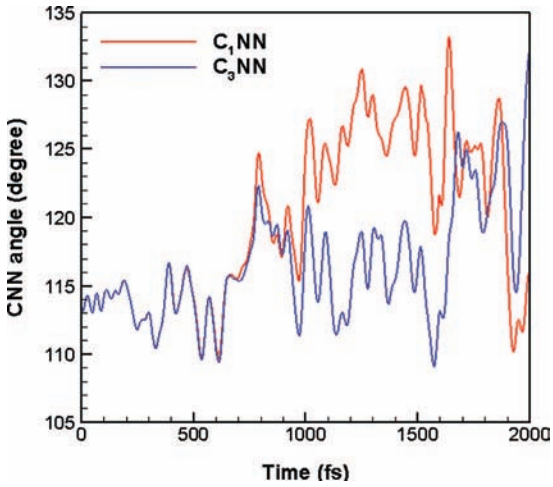

Figure 5. Changes in the two CNN angles of *E*-Ab subjected to a 50 fs (fwhm) laser pulse with a fluence of 0.459 kJ/m^2 and photon energy of 1.75 eV. The laser pulse generates the nπ* excitation.

becomes smaller than 20°. The molecule then fluctuates about this dihedral angle by the end of the simulation time. On the other hand, only substantial rotation about either of the C−N bonds is found until 1600 fs. After this time, one of the phenyl rings rotates to about 60°. This torsion finally goes back to about 180°. Two C−C−N−N dihedral angles then oscillate about 180° in the rest of the simulation time. The energy for activating the C−C−N−N torsional motion must come from the release of electronic energy during the nonadiabatic transition at 1600 fs. The torsional angle variations clearly demonstrate that the reaction follows the rotational path.

The variations of two CNN bond angles with time are presented in Figure 5. Both bond angles swing about their original value of 114° before 630 fs. The C_1NN angle expands significantly after 630 fs when the molecule starts to rotate about its central bond. On the other hand, the C_3NN angle has a relatively small expansion after 630 fs. Two bond angles finally come to about 120° after the *Z*-isomer is produced. It is found that the C_1NN angle widens to as large as 136° at 975 fs. However, no linear geometry is observed for any CNN bond bending angles, indicating the reaction does not follows the inversion path.

The bond length variations of the N−N and two C−N bonds with time are plotted in Figure 6. Quickly following the laser irradiation, the N−N bond lengthens from about 1.29 Å to an average length of 1.46 Å. It remains about this length by 610 fs and then shortens to about 1.32 Å by 1000. The N−N bond then stays at this length for the rest of the simulation time. On the other hand, following the application of the laser pulse, two C−N bonds speedily shorten to about 1.35 Å. They have this length on average as far as 1000 fs. Two C−N bonds stretch to about 1.41 Å on average after 1500 fs and then oscillate about this length until the end of the simulation.

2. $\pi\pi$* Excitation. A laser pulse of 50 fs (fwhm) with an effective photon energy of 2.2 eV and a fluence of 0.189 kJ/m^2 is applied to produce $\pi\pi$* excitation.

The time-dependent populations of the HOMO−1, HOMO and LUMO are presented in Figure 7. Figure 7a is an expanded scale of Figure 7b from 0 to 100 fs. The laser pulse brings about 1.6 electrons to the LUMO by 20 fs and leaves a hole mainly at the HOMO−1. At about 20 fs, a sharp electronic population transfer moves holes from the HOMO−l to HOMO. When the laser pulse ends, about 1.6 electrons are in the LUMO and holes stay in the HOMO. Several noticeable electronic transitions

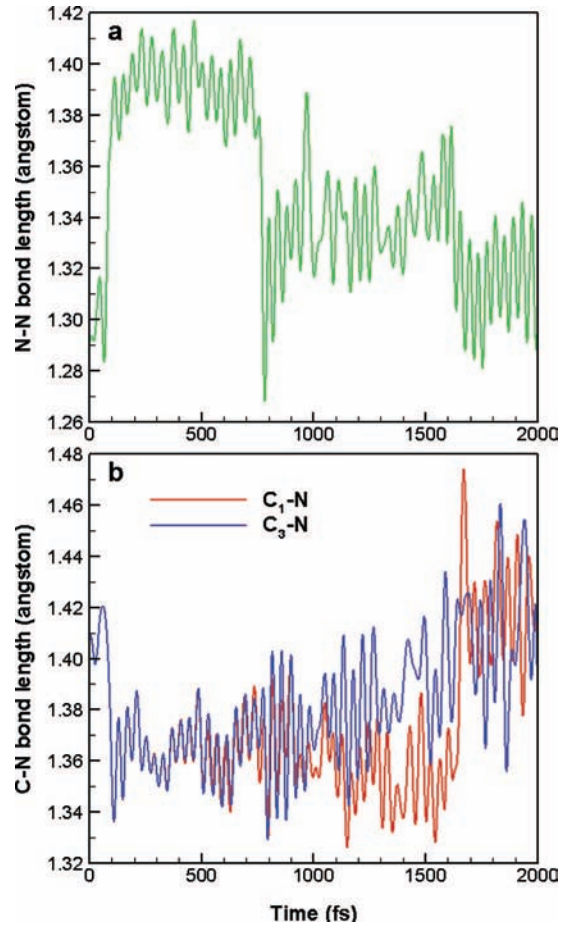

Figure 6. Variations during laser pulse excitation in (a) the N−N bond length and (b) two C−N bond lengths of *E*-Ab. The 50 fs (fwhm) laser pulse has a fluence of 0.459 kJ/m^2 and photon energy of 1.75 eV and induces the nπ* excitation.

occur between the LUMO and HOMO. It is found that the electronic transitions at about 510, 820, and 1291 fs bring electrons from the LUMO to HOMO and others move electrons from the HOMO to the LUMO. After 1300 fs, the molecule essentially moves at the electronic ground-state as the majority of excited electrons come back to the HOMO.

The variations with time of the energies of the HOMO−1, HOMO and LUMO are plotted in Figure 8 with an expanded scale from 0 to 100 fs shown in Figure 8a. An avoided crossing is found between the HOMO−1 and HOMO at about 20 fs. This avoided crossing leads to the electronic transition from the HOMO to HOMO−1, as shown in Figure 7a. Multiple avoided crossings between the HOMO and LUMO are found from 510 to 1300 fs and they are responsible to the electronic transitions between the two orbitals, as shown in Figure 7b.

Six snapshots from the simulation at different times for this reaction path are shown in Figure 9. Following the laser excitation, *E*-Ab rotates about the central bond after 370 fs. After the CNNC dihedral angle reaches about 90° at 814 fs. The molecule then twists back, avoiding the isomerization. It becomes the *E* geometry after 1600 fs.

The variations of three torsional angles with time are plotted in Figure 10. Although both CCNN torsional angles slightly vibrate about their initial value soon after the laser pulse is applied, no obvious changes are found in the CNNC torsional angle before 370 fs. The CNNC dihedral angle starts to decrease after 400 fs and drops to 140° at 514 fs. After a flat variation before 720 fs, it quickly goes down to 98° at 814 fs. The CNNC

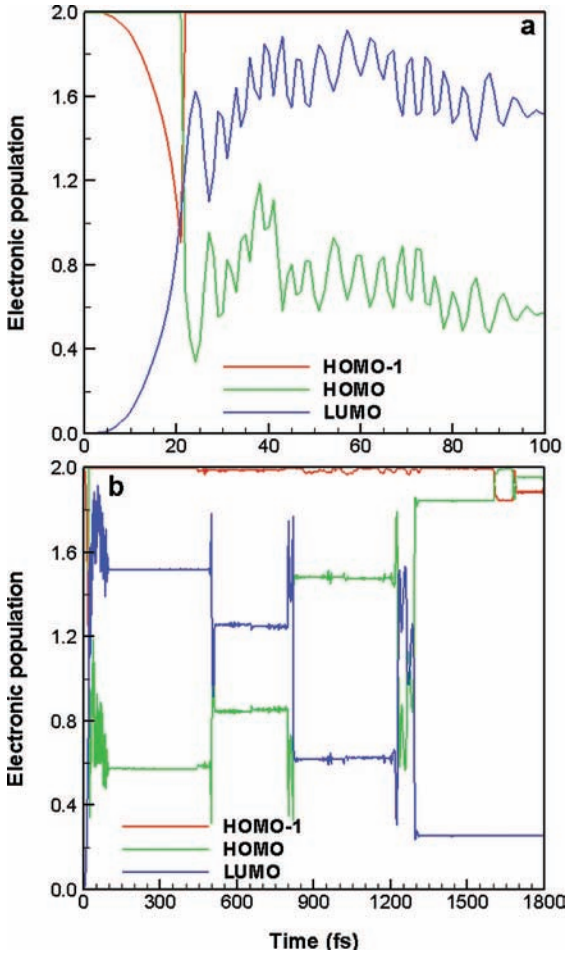

Figure 7. Variation with time of the electronic populations of the HOMO−1, HOMO, LUMO of *E*-Ab following application of a 50 fs (fwhm) laser pulse with a fluence of 0.189 kJ/m^2 and photon energy of 2.2 eV. The laser pulse produces the $\pi\pi^*$ excitation. (b) is an expanded scale of a from 0 to 100 fs.

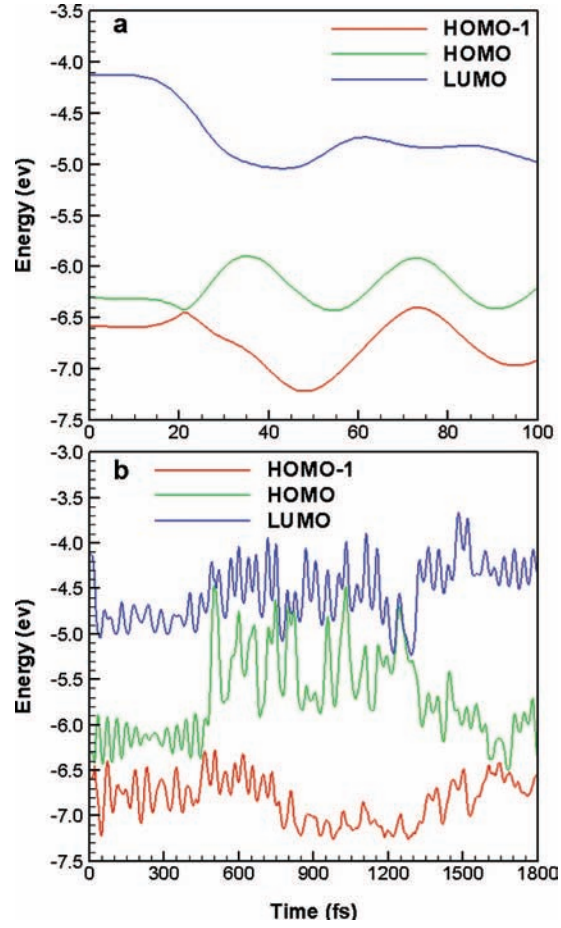

Figure 8. Energy variation with time of the HOMO−1, HOMO and LUMO of EAb following application of a 50 fs (fwhm) laser pulse with a fluence of 0.189 kJ/m^2 and photon energy of 2.2 eV. The reaction is triggered by the $\pi\pi^*$ excitation. (b) is an expanded scale of a from 0 to 100 fs.

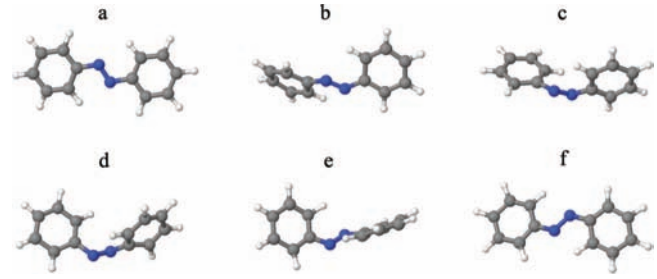

Figure 9. Six snapshots taken from the simulation of *E*-Ab responding to a 50 fs (fwhm) laser pulse with a fluence of 0.189 kJ/m^2 and photon energy of 2.2 eV at (a) 0 fs, (b) 520 fs, (c) 830 fs, (d) 1240 fs, (e) 1362 fs, and (f) 1620 fs. The simulation follows the $\pi\pi^*$ excitation.

torsional angle rises and falls between 90° and 140° until 1300 fs and then goes back to about 180°. It reaches about 180° at 1600 fs when the *E* geometry is formed. On the other hand, only small variations are found in two CCNN dihedral angles during the simulation process.

The variations of CNN bond angles with time are presented in Figure 11. Both bond angles oscillate about their original value of 114° before 440 fs. However, it is noticed that both CNN bending vibrations have greater amplitude soon after the laser pulse is applied. They sharply rise up to as large as 137° soon after 450 fs. Two band angles drop down after 830 fs and come to about their beginning value after 1300 fs. However, the amplitudes of the bond bending vibrations are much greater after then.

The bond length variations of the N−N and two N−C bonds with time are presented in Figure 12. Figure 12a shows that immediately after the laser excitation, the N−N bond stretches from 1.29 Å to an average length of 1.45 Å, a typical value for a single N−N bond. It keeps this length before 440 fs. The N−N bond is sharply compressed to about 1.3 Å after 500 fs and holds this length over the remainder of the simulation time. In contrast, two C−N bonds become shorter soon after the laser pulse is applied. Both bonds start to lengthen after 600 fs and come back to about 1.4 Å after 1400 fs. They both oscillate about this length for the rest of the simulation time.

For the $\pi\pi^*$, the laser pulse excites *E*-Ab to the S($\pi\pi^*$) state. The ultrafast electronic transfer at about 20 fs is immediately followed by $(\pi)^2(\pi^*)^2$ excitation, indicating that the excited molecule decays from the S($\pi\pi^*$) state to the S($(\pi)^2(\pi^*)^2$) state. The decay time of 20 fs is comparable to the experimentally observed lifetime of less than 100 fs for the S($\pi\pi^*$) state. Some important geometrical parameters at the S($\pi\pi^*$)/S($(\pi)^2(\pi^*)^2$) decay are CNNC = 180°, CCNN = NNCC = 180°, CNN = NNC = 112°, NN ≈ 1.42 Å, and CN = NC ≈ 1.30 Å. These parameters are in good agreement with those obtained by CASSCF/CASPT2 calculation[44] and also with experimental finding[21] that the molecule after the S($\pi\pi^*$) decay has a planar structure with the NN bond enlarged.

By performing CASSCF/CASPT2 calculation,[24] Conti et al. find that the S($(\pi)^2(\pi^*)^2$) MEP is essentially degenerate with a

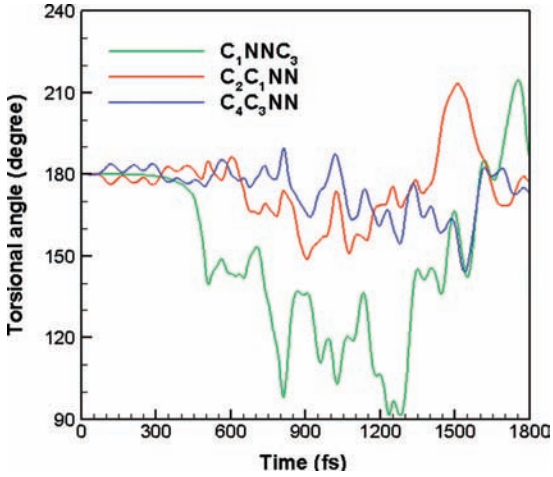

Figure 10. Variations with time of the three torsional angles of *E*-Ab subjected to a 50 fs (fwhm) laser pulse with a fluence of 0.189 kJ/m^2 and photon energy of 2.2 eV. This laser pulse induces the $\pi\pi^*$ excitation.

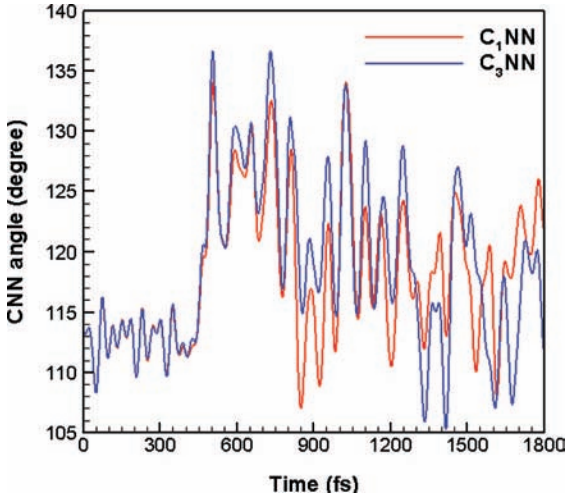

Figure 11. Changes in two CNN angles of *E*-Ab subjected to a 50 fs (fwhm) laser pulse with a fluence of 0.189 kJ/m^2 and photon energy of 2.2 eV. The laser pulse produces the $\pi\pi^*$ excitation.

seam of S($\pi\pi^*$)/S(nπ^*) conical intersections and that CNN bending vibrations may provide an efficient approach for the excited molecule to decays to the S(nπ^*) state. Our simulation finds that for the $\pi\pi^*$ excitation the first decay channel after moving on the S(nπ^*) state occurs at about 510 fs and about 0.4 electrons are transferred from the LUMO to HUMO at this deexcitation. Although the present Ehrenfest approach does not describe a complete de-excitation picture at this time, the solution of the time-dependent Schrödinger equation does indicate that there exists a potential nonadiabatic decay channel at this geometry. The molecular geometry with some important parameters indicated at this time is shown in Figure 13. This decay channel is characterized by the geometrical parameter CNNC = 139.4°, CNN = 133.7° and NNC = 135.5°. The excited molecule decays to the S_0 state through this channel will have a partially twisting structure and not isomerizes.

Multiple S(nπ^*)/S_0 decay channels found from 700 to 1300 fs occur at around twisted, the CNNC close to 90°, structure. Few of representative geometries are presented in Figure 14 with some main geometrical parameters indicated. It is seen that each of these geometries has a roughly twisted structure with CNNC = 98.3°, 92.9°, and 93.5°, respectively. The existence of multiple decay channels from the S_1 state to the S_0

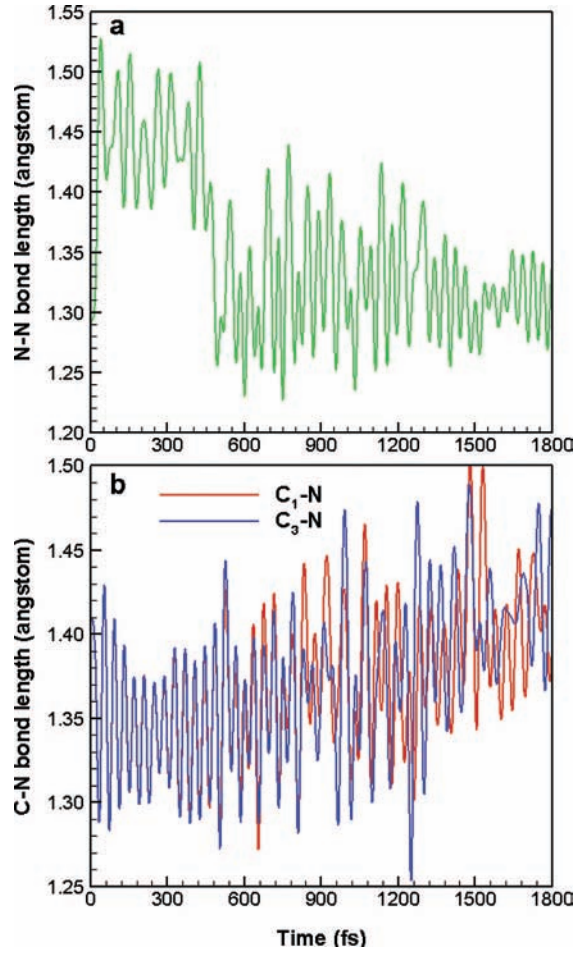

Figure 12. Variations during laser pulse excitation in (a) the N−N bond length and (b) the two C−N bond lengths of EAb subjected to a 50 fs (fwhm) laser pulse with a fluence of 0.189 kJ/m^2 and photon energy of 2.2 eV. This is the $\pi\pi^*$ excitation.

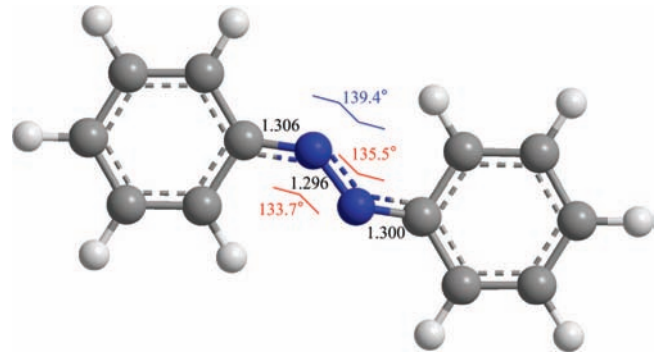

Figure 13. Molecular geometry taken at t = 510 fs in the simulation for the $\pi\pi^*$ excitation.

state at about the perpendicular structure of two phenyl rings in the Ab has been reported by the Cembran et al.[23] These authors identified several lowest energy S_1/S_0 conical intersections close to the twisted region of Ab by performed CASPT2 calculation. A decay channel at about twisted structure leads to the formation of either the *E*- or *Z*-isomer, which is one accounting for the isomerization quantum yield observed for $\pi\pi^*$ excitation. For example, the decay channel that the reaction following in the presented trajectory leads to the formation of the reactant. The existence of a decay channel at a geometry far from the twisted structure accounts for the poor *E*−*Z* photoisomerization quantum yield for $\pi\pi^*$ excitation.

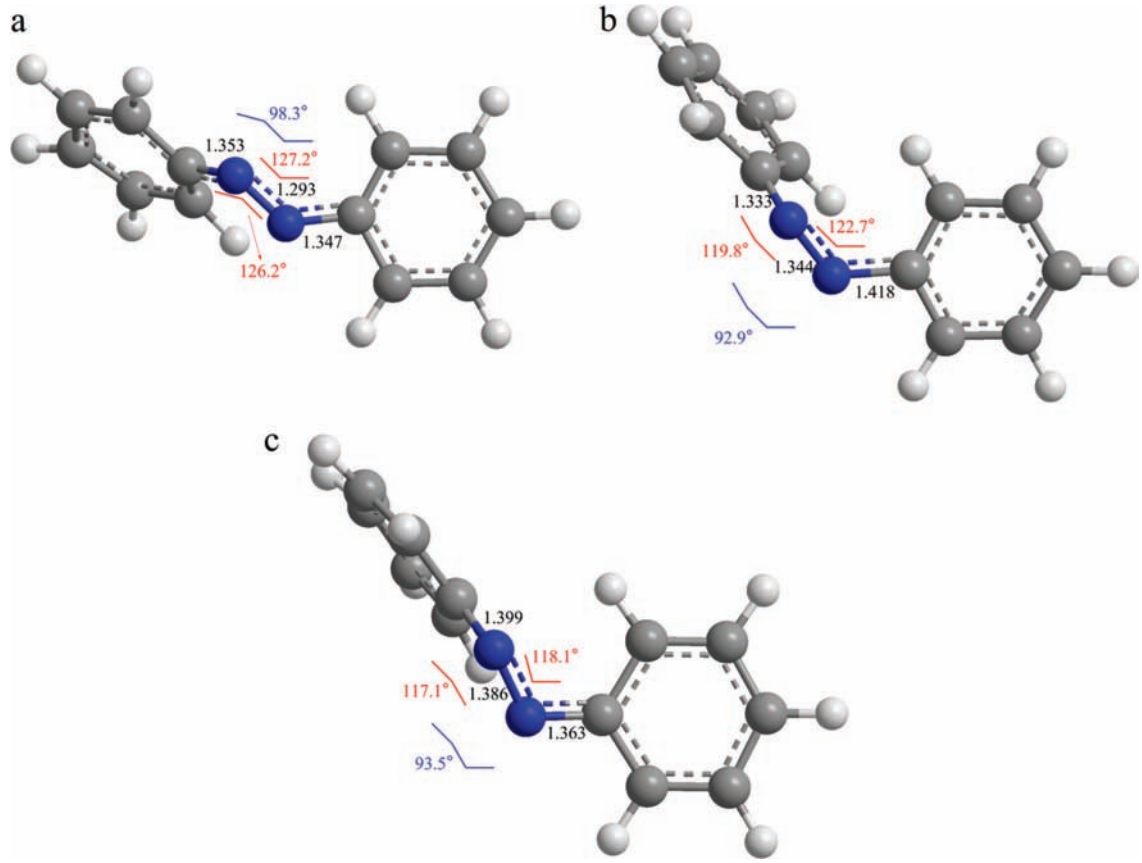

Figure 14. Molecular geometries taken at t = (a) 820 fs, (b) 1230 fs, and (c) 1292 fs, respectively, in the simulation for the $\pi\pi^*$ excitation.

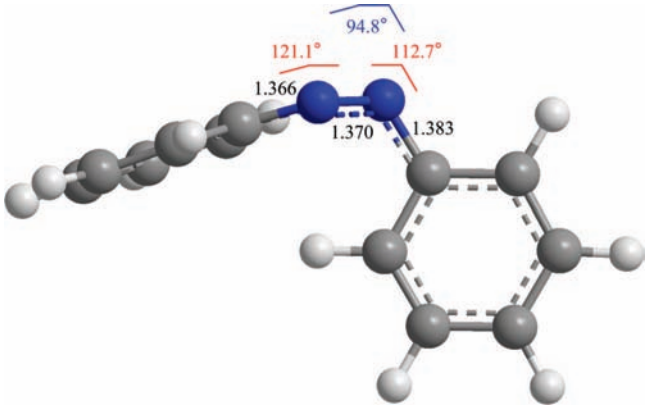

Figure 15. Molecular geometry taken at t = 1610 fs in the simulation for the nπ^* excitation.

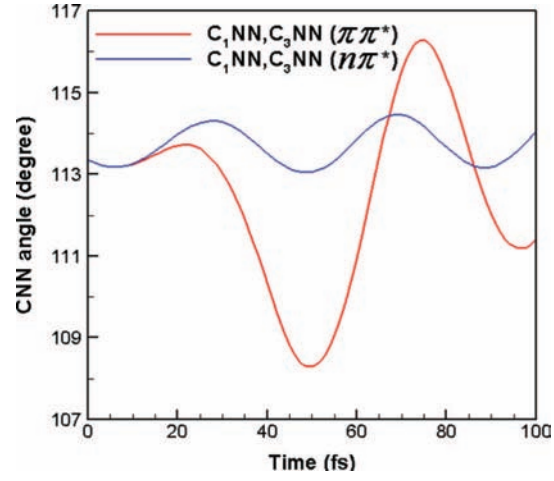

Figure 16. Comparison of the CNN bond angles between the nπ^* and $\pi\pi^*$ excitations.

For nπ^* excitation, the excited molecule finds S(nπ^*)/S_0 decay channel only at about twisted structure, as shown in Figure 15. This decay channel is presented by the geometrical parameter CNNC = 94.8°, CNN = 121.1° and NNC = 112.7°. This decay channel leads the reaction toward either the product or the reactant. Experimentally observed larger photoisomerization quantum yield for nπ^* excitation than for $\pi\pi^*$ excitation can be explained by disappearance of the S(nπ^*)/S_0 decay channel at a partially twisted structure in the former excitation. The existence of this decay channel favors the formation of the reactant.

Examining the variations of different vibrational modes for $\pi\pi^*$ excitation finds that the CNN bond bending vibrations are significantly excited after the S($\pi\pi^*$)/S($(\pi)^2(\pi^*)^2$) decay at about 20 fs, as shown in Figure 16 compared to those for nπ^* excitation. The energy for this excitation comes from internal energy conversion at the S($\pi\pi^*$)/S($(\pi)^2(\pi^*)^2$) decay. For nπ^* excitation, on the other hand, the CNN bond bending vibration shows about the same amplitude after the laser pulse is applied. The excitation of the CNN bond bending vibrational mode facilitates the CNN angles widening. The opening of the CNN angles, combining with the CNNC torsion, makes the coupling between the HOMO and LUMO at about 510 fs which eventually leads to the S(nπ^*)/S_0 decay. Figure 17 demonstrates the effect of the CNN angles widening on the HOMO−LUMO coupling at 510 fs. The fact that the CNN bond bending vibration peaks coincide with the avoided crossings between the HOMO−LUMO at about 510 fs indicates involvement of the CNN bond bending vibration in the couplings between these orbitals.

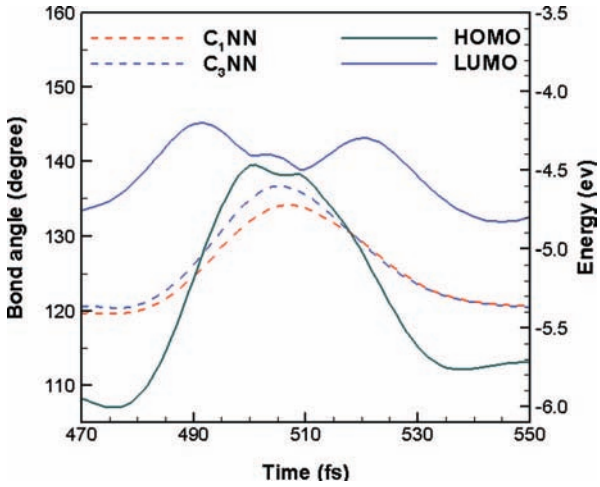

Figure 17. Effect of the CNN angle variations on the HOMO and LUMO coupling at the partially twisted geometry for the $\pi\pi^*$ excitation.

In conclusion, in the $\pi\pi^*$ excitation the decay of the excited molecule at $S(\pi\pi^*)/S((\pi)^2(\pi^*)^2)$ makes the CNN bond bending vibration excited. This excitation promotes the CNN bond angles expanded. The expansion of the CNN angles makes significant contribution to the decay channel at the geometry far from the twisted structure. This decay channel leads to the formation of the *E*-isomer and account for experimentally observed smaller quantum yield for the $E-Z$ photoisomerization of Ab for the $\pi\pi^*$ excitation than for the $n\pi^*$ excitation.

Conclusions

In this publication, we have presented detailed simulation results for the isomerization of *E*-Ab. The simulation follows two excitations, namely $n\pi^*$ excitation characterized by the HOMO to LUMO transition, and $\pi\pi^*$ excitation characterized by the HOMO−1 to LUMO transition. Two excitations are triggered by two 50 fs (fwhm) laser pulses which are different in the photon energies. For the $n\pi^*$ excitation, the simulation finds a nonadiabatic decay at the twisted structure and this decay leads to the formation of the *Z* isomer. For the $\pi\pi^*$ excitation, the simulation shows a nonadiabatic decay at a partially twisted structure and multiple decay channels at about the twisted structure. The decay at the partially twisted structure favors the formation of the *E*-isomer, which lowers the $E-Z$ quantum yield. The decay close to the twisted structure may guide the reaction to either the product or the reactant. In the trajectory presented, *E*-Ab is formed. The detailed examination of the decay at the partially twisted structure indicates that the CNN/NNC bond bending vibrations are strongly involved in the LUMO−HOMO coupling for the partially twisted structure decay. The CNN/NNC bond bending vibrations are excited by the internal energy at the decay of the $S(\pi\pi^*)$ but do not show notable activation for the $n\pi^*$ excitation.

Finally it is worth noting that the simulation results demonstrate that the geometry changes of *E*-Ab at the electronically excited state in the initial process of photoisomerization mainly involve the CN and NN lengths and CNN bond angles. The remarkable changes in the torsions, for example in the $n\pi^*$ excitation, only occur in the last less than 400 fs. The recent Resonance Raman spectroscopic experiment by Mathies's group[15] suggests that the excited-state geometry changes of *E*-Ab are primarily focused on the CNN band and CN and NN stretches and they therefore conclude that for the $n\pi^*$ excitation the reaction coordinate is predominated by the inversion path. This conclusion does not entirely agree with the statement we made above.

Acknowledgment. We acknowledge support by the National Natural Science Foundation of China (Grant 20773168) and Research Fund of Chongqing University of Posts and Telecommunications (A2006-81), and acknowledgment is also made to the donors of The American Chemical Society Petroleum Research Fund for support of this research at Nicholls State University.

Supporting Information Available: Geometries (xyz format) produced in the simulations for both excitations at every 0.05 fs and an animation file for each reaction are available free of charge via the Internet at http://pubs.acs.org.

References and Notes

(1) Ikeda, T.; Tsutsumi, O. *Science* **1995**, *268*, 1873.
(2) Shipway, A. N.; Willner, I. *Acc. Chem. Res.* **2001**, *34*, 421.
(3) Liu, Z. F.; Hashimoto, K.; Fujishima, K. *Nature* **1990**, *347*, 658.
(4) Hugel, T.; Holland, N. B.; Cattani, A.; Moroder, L.; Seitz, M.; Gaub, H. E. *Science* **2002**, *296*, 1103.
(5) Rau, H. In *Photochromism, Molecules and System*; Durr, H., Bouas-Laurent, H., Eds.; Elsevier: Amsterdam, 1990; Vol 1, Chapter 4, pp 165−192, and references therein.
(6) Siampiringue, N.; Guyot, G.; Bortolus, P.; Mouti, S. *J. Photochem.* **1987**, *37*, 185.
(7) Bortolus, P.; Monti, S. *J. Phys. Chem.* **1979**, *83*, 648.
(8) Rau, H.; Lueddecke, E. *J. Am. Chem. Soc.* **1982**, *104*, 1616.
(9) Schultz, T.; Quenneville, J.; Levine, B.; Toniolo, A.; Martinez, T. J.; Lochbrunner, S.; Schmitt, M.; Shaffer, J. P.; Zgierski, M. Z.; Stolow, A. *J. Am. Chem. Soc.* **2003**, *125*, 8098.
(10) Tamai, N.; Miyasaka, H. *Chem. Rev.* **2000**, *100*, 1875.
(11) Nägele, T.; Hoche, R.; Zinth, W.; Wachtveitl, J. *Chem. Phys. Lett.* **1997**, *272*, 489.
(12) Lednev, I.; Ye, T. Q.; Matousek, P.; Townie, M.; Foggi, P.; Neuwahl, F.; Umapathy, S.; Hester, R.; Moore, *Chem. Phys. Lett.* **1998**, *290*, 68.
(13) Lednev, I. K.; Ye, T.-Q.; Abbott, L. C.; Hester, R. E.; Moore, J. N. *J. Phys. Chem. A* **1998**, *102*, 9161.
(14) Hirose, Y.; Yui, H.; Sawada, T. *J. Phys. Chem. A* **2002**, *106*, 3067.
(15) Stuart, C. M.; Frontiera, R. R.; Mathies, R. A. *J. Phys. Chem. A* **2007**, *111*, 12072.
(16) Tiago, M. L.; Ismail-Beigi, S.; Louie, S. G. *J. Chem. Phys.* **2005**, *122*, 0943111.
(17) Gagliardi, L.; Orlandi, G.; Bernardi, F.; Cembran, A.; Marco Garavelli, M. *Theor. Chem. Acc.* **2004**, *111*, 363.
(18) Ishikawa, T.; Noro, T.; Shoda, T. *J. Chem. Phys.* **2001**, *115*, 7503.
(19) Cembran, A.; Bernardi, F.; Garavelli, M.; Gagliardi, L.; Orlandi, G. *J. Am. Chem. Soc.* **2004**, *126*, 3234.
(20) Lednev, I.; Ye, T. Q.; Hester, R.; Moore, J. *J. Phys. Chem.* **1996**, *100*, 13338.
(21) Fujino, T.; Arzhantsev, S. Yu.; Tahara, T. *J. Phys. Chem. A* **2001**, *105*, 8123.
(22) Chang, C. W.; Lu, Y.-C.; Wang, T.-T.; Diau, E. W.-G. *J. Am. Chem. Soc.* **2004**, *126*, 3234.
(23) Cembran, A.; Bernardi, F.; Garavelli, M.; Gagliardi, L.; Orlandi, G. *J. Am. Chem. Soc.* **2004**, *126*, 3234.
(24) Conti, I.; Garavelli, M.; Orlandi, G. *J. Am. Chem. Soc.* **2008**, *130*, 5216.
(25) Dou, Y.; Torralva, B. R.; Allen, R. E. *J. Mod. Opt.* **2003**, *50*, 2615.
(26) Dou, Y.; Torralva, B. R.; Allen, R. E. *Chem. Phys. Lett.* **2004**, *392*, 352.
(27) (a) Graf, M.; Vogl, P. *Phys. ReV. B.* **1995**, *51*, 4940. (b) See also Boykin, T. B.; Bowen, R. C.; Klimeck, G. *Phys. Rev. B* **2001**, *63*, 245314.
(28) Porezag, D.; Frauenheim, Th.; Kohler, Th.; Seifert, G.; Kaschner, R. *Phys. Rev. B* **1995**, *51*, 12947.
(29) Elstner, M.; Porezag, D.; Jungnickel, G.; Elsner, J.; Haugk, M.; Frauenheim, Th.; Suhai, S.; Seifert, G. *Phys. Rev. B* **1998**, *58*, 7260.
(30) Porezag, D.; Frauenheim, Th.; Kohler, Th.; Seifert, D.; Kaschner, R. *Phys. Rev. B* **1995**, *51*, 12947.
(31) Torralva, B. R.; Niehaus, T. A.; Elstner, M.; Suhai, S.; Frauenheim, Th.; Allen, R. E. *Phys. Rev. B* **2001**, *64*, 153105.
(32) Dou, Y.; Lei, Y.; Li, A.; Wen, Z.; Torralva, B. R.; Lo, G. V.; Allen, R. E. *J. Phys. Chem. A* **2007**, *111*, 1133–1137.
(33) Dou, Y.; Allen, R. E. *J. Chem. Phys.* **2003**, *19*, 10658–10666.
(34) Ben-Nun, M.; Martínez, T. J. *Adv. Chem. Phys.* **2002**, *124*, 439.

(35) Allen, R. E.; Dumitrica, T.; Torralva, B. R. In *Ultrafast Physical Processes in Semiconductors*; Tsen, K. T., Ed.; Academic Press: New York, 2001; Chapter 7.

(36) Born, M.; Oppenheimer, J. R. *Ann. Phys. (Leipzig)* **1927**, *84*, 457.

(37) Born, M., Huang, K. *The Dynamical Theory of Crystal Lattices*; Oxford University Press: London, 1954.

(38) Teller, E. *J. Phys. Chem.* **1937**, *41*, 109.

(39) *Conical Intersections: Electronic Structure, Dynamics, and Spectoscopy*; Domcke, W., et al., Eds.; World Scientific: Singapore, 2004.

(40) Baer, M. *Beyond Born-Oppenheimer: Electronic Nonadiabatic Coupling Terms and Conical Intersections*; Wiley Interscience: Hoboken, NJ, 2006.

(41) Bearpark, M. J.; Bernardi, F.; Clifford, S.; Olivucci, M.; Robb, M. A.; Vreven, T. *J. Phys. Chem. A* **1997**, *101*, 3841.

(42) Levine, B. G.; Martínez, T. J. *Annu. Rev. Phys. Chem.* **2007**, *58*, 613.

(43) Toniolo, A.; Levine, B.; Thompson, A. L.; Quenneville, J.; Ben-Nun, M.; Owens, J.; Olsen, S.; Manohar, L.; Martinez, T. J. In *Computational methods in organic photochemistry*; Kutateladze, A., Ed.; Marcel-Dekker: New York, 2005.

(44) Cattaneo, P.; Persico, M. *Phys. Chem. Chem. Phys.* **1999**, *1*, 479.

(45) Ishikawa, T.; Noro, T.; Shoda, T. *J. Chem. Phys.* **2001**, *115*, 7503.

(46) Ciminelli, C.; Granucci, G.; Persico, M. *Chem. Eur. J.* **2004**, *10*, 2327.

JP806227X